Fabrication and Electrocatalytic Performance of a Two-Dimensional β-PbO₂ Macroporous Array for Methyl Orange Degradation

Song Yuzhu, Chen Zhen, Gui Lai, Yu Qiang, Zhu Wei, Wu Dan, and Zheng Tao*

Faculty of science, Kunming University of Science and Technology, Kunming 650093, People's Republic of China
*E-mail: chenzhen69@qq.com, songyuzhu1@foxmail.com

To further improve the electrocatalytic degradation activity of PbO_2 electrodes for refractory organic pollutant treatment, a novel two-dimensional β-PbO_2 macroporous array electrode (2D-PbO_2) was fabricated by electrochemical deposition based on a two-dimensional colloidal crystal template, which was constructed using the Langmuir-Blodgett film technique. The structure and surface morphology of 2D-PbO_2 electrodes and traditional flat electrodes (Flat-PbO_2) were characterized by scanning electron microscopy (SEM) and X-ray diffraction (XRD). The anode polarization curves, cyclic voltammetry (CV) curves and electrochemical impedance spectroscopy (EIS) measurements were investigated to compare the electrocatalytic activity of the two kinds of electrodes. The electrocatalytic degradation of methyl orange (MO) was performed by CV, and UV spectroscopy was used to monitor changes during the electrocatalytic degradation process. The results show that the as-prepared electrode exhibited a two-dimensional ordered micron spherical cavity array structure with a large specific surface area. The coating surface is composed of single β-PbO_2 microcavities 5-6 μm in size, and the spacing of the micron holes is approximately 2 μm. Compared with the Flat-PbO_2 electrodes, the 2D-PbO_2 electrodes show a higher exchange current density (j^0=1.478×10⁻⁵ A·cm⁻²), smaller apparent activation energy (E_a=12.09 kJ·mol⁻¹), larger electric double layer capacitance (C_{dl}=60 μF·cm⁻²) and smaller charge transfer resistance (R_{ct}=16.89 Ω·cm²), resulting in better electrocatalytic performance. In the electrocatalytic degradation process of MO, the conjugated chromophore group in the molecular structure of MO has been damaged by direct oxidation methods. The reaction followed pseudo first-order kinetics, and the value of the apparent rate constant (k_{app}) is 0.06814 min⁻¹, approximately 2.35 times that of the Flat-PbO_2 electrodes (0.02902 min⁻¹). The electrocatalytic degradation efficiency was significantly improved.

Keywords: 2D-PbO_2 electrodes; Langmuir-Blodgett films technique; electrocatalytic degradation; methyl orange

1. INTRODUCTION

The rapid development of the textile and printing industries, while improving the quality of human life, has also caused damage to our environment, forcing the human society to face enormous water resource challenges. The proportion of azo substances in dye wastewater is the largest, and these substances have the characteristics of large chroma, carcinogenicity and refractory degradation, which makes the degradation of azo dye wastewater one of the difficult problems in industrial wastewater treatment. For the degradation of azo substances, traditional wastewater treatment methods can be divided into physical methods, chemical methods, biological methods and advanced oxidation methods[1]. Electrocatalytic oxidation technology[2-3], one of the organic wastewater treatment methods gradually developed in the 1980s, has the advantages of simple equipment, mild reaction conditions, easy automation and no secondary pollution and has attracted researchers' attention. The electrode materials play significant roles in the electrochemical oxidation process, and their performance is the key to industrial application.

In recent years, quantities of electrode materials have been fabricated, such as PbO_2[4-8], SnO_2[9] and BBD[8]. Among these electrode materials, PbO_2 electrode materials have become one of the most widely studied and applied anode materials for the treatment of biodegradable organic wastewater due to their advantages of low production cost, high current efficiency, excellent corrosion resistance and electrocatalytic ability. To improve the electrochemical properties of PbO_2 electrodes, the main focus has been on many aspects, such as the substrate, bottom and middle layers, surface layer doping, process preparation conditions and deposition mechanisms [9-12]. Among them, one of the hotspots to improve electrocatalytic performance is by directly increasing the electrochemical active surface area of the electrodes. Research shows that[12-16] Langmuir-Blodgett films (LB films) are a monomolecular membrane assembly technique pioneered by L. Langmuir and K. Blodgett. At the gas-liquid interface, amphiphilic molecules with a hydrophilic head and hydrophobic tail are dispersed on the surface of the liquid phase, and then surface active substances are injected to change the surface tension of water, thereby causing the molecules to be closely arranged in an orderly manner to form a single monomolecular membrane (Langmuir film). Then, when the solid substrate is immersed or removed from the liquid phase, the L film can be transferred from the liquid phase to the surface of the matrix to obtain an LB film.

In research on nanometer functional materials[15-23], the LB film technique was used to assemble micro-/nano-particles such as polystyrene (PS) microspheres or SiO_2 onto the surface of a solid substrate to obtain two-dimensional or three-dimensional colloidal crystal templates. Electrochemical deposition was carried out based on this template, and the functional materials were embedded into the gap of the template. After removing the colloidal crystal template, functional materials with a two-dimensional or three-dimensional reversed-phase spherical cavity array could be obtained. The template has the characteristics of accurate dimensionality control through the number of layers of LB films, few array structure defects and simple preparation operations.

Therefore, this research aimed to examine the problem of the low efficiency of PbO_2 electrical catalytic degradation. First, a stainless-steel substrate two-dimensional colloidal crystal template was prepared, and then based on this template, two-dimensional porous array structure β-PbO_2 electrodes

were prepared by an anodic oxidation method. The electrode array structure can effectively increase the specific surface area and the active sites, thus increasing the load of the active material. This can improve the electrocatalytic performance of the active layer of the electrode and realize efficient degradation of MO.

2. EXPERIMENTAL

2.1 Electrode preparation

The 2D-PbO$_2$ electrodes were fabricated by a combination of the anodic oxidation method and LB film technique to construct a two-dimensional colloidal crystal template[18-20]. The 2D-PbO$_2$ electrodes were prepared in four steps, and the protocol is schematically illustrated in Figure 1. The stainless-steel substrate with a two-dimensional colloidal crystal template served as the anode (10 mm×50 mm×1 mm) after polishing, degreasing, acid activation, and ethanol absolute (AR) preservation. Before the preparation of the two-dimensional colloidal crystal templates, the surface of the pretreated substrate was cleaned with acetone via ultrasonic cleaning, ethanol absolute ultrasonic cleaning, deionized water washing, drying and other processes for surface decontamination and hydrophilic treatment. A stainless-steel substrate with the same area was used as the cathode. The composition of the plating bath was Pb(NO$_3$)$_2$ 190.0 g·L^{-1}, NaF 0.5 g·L^{-1}, Cu(NO$_3$)$_2$ 15.0 g·L^{-1}, pH=2-3. The operating conditions were as follows: average current density of 5 mA·cm^{-2}, bath temperature of 40°C, and electrodeposition time of 16 minutes.
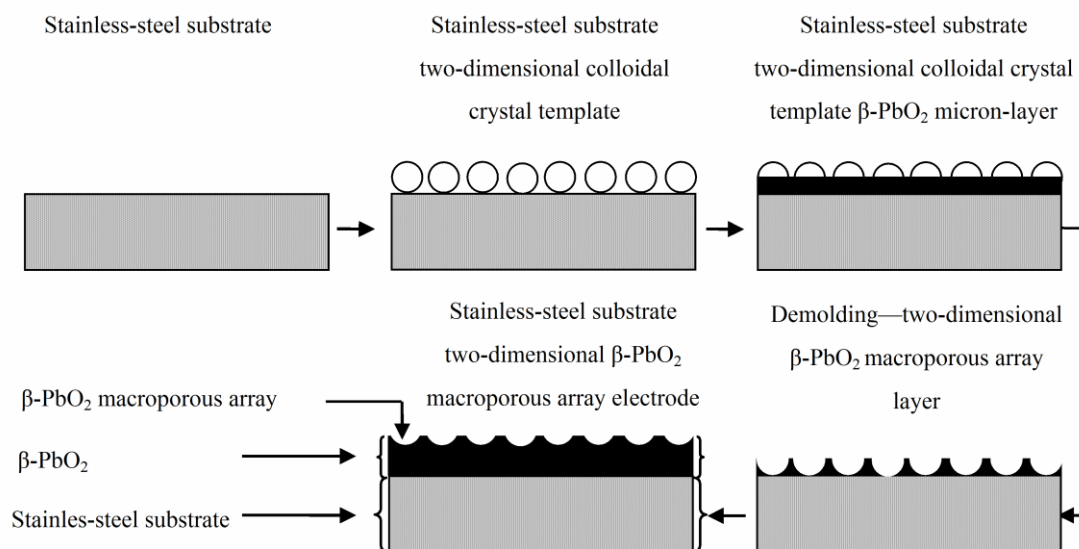
Figure 1. Schematic illustration of the fabrication of the stainless-steel substrate two-dimensional β-PbO$_2$ macroporous array electrodes.

2.1.1 Preparation of the stainless-steel substrate two-dimensional colloidal crystal templates

1. Preparation of PS microsphere monodispersed layer: First, 2 mL of a monodispersed emulsion containing PS microspheres (the weight to volume ratio of 2.5%) with a particle size of 8 μm

and 1.5 mL absolute ethanol were combined in a beaker and subjected to ultrasonic dispersal for 3 minutes. Then, an appropriate amount of the above mixed emulsion was syringe injected at a rate of 0.5 mL·h⁻¹ and to a beaker containing 200 mL of ultrapure water so that the PS microspheres could spread into a single layer film at the air-water interface. After standing for 3 minutes, a solution of 0.05 mL sodium dodecylbenzenesulfonate solution (SDS, mass fraction of 0.1%) was injected from the edge of the beaker to form a stable PS microsphere monodispersed layer for later use.

2. Preparation of the stainless-steel substrate two-dimensional colloidal crystal templates: The stainless-steel substrate was vertically and completely inserted into the PS microsphere monodispersed layer and then slowly pulled out at a constant speed and dried naturally. After constant temperature drying at 90°C for 30 minutes, the stainless-steel substrate two-dimensional colloidal crystal template was obtained, and the gas-solid interface for the process is shown in Figure 2. The basic principle of the method[13, 16, 17, 19] is continuous evaporation of the solvent on the surface of the substrate with the pulling of the substrate. At this time, the synergistic effect of the surface tension of the PS microspheres in the water and the infiltration force caused by the convex surfaces close to each other is gravitation, which promotes the movement of the PS microspheres toward the substrate to become a "nucleus". When the pulling speed of the substrate is slower than the evaporation rate of the solvent at the meniscus of the PS microspheres, the moisture of the meniscus is rapidly reduced, and the external moisture is brought closer to the crystal nucleus. Under the action of convective transport and gravity, the "growth" arrangement of the microspheres is driven as the solvent evaporates, and the colloidal spheres are arranged close together one by one, causing the nucleus to grow and form colloidal crystals. The two-dimensional colloidal crystals have an ordered close-packed hexagonal structure on the surface of the substrate, as shown in Figure 3a.
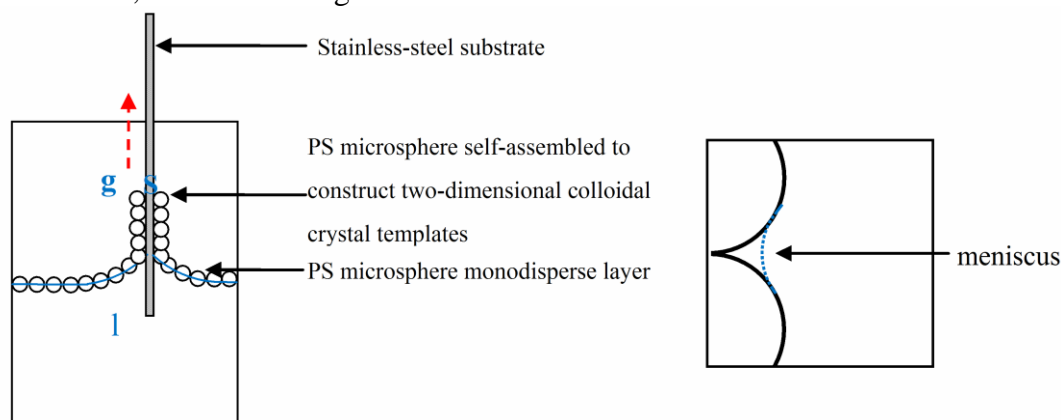
Figure 2. Formation of two-dimensional colloidal crystal templates at the gas-solid interface.

2.1.2 Preparation of stainless-steel substrate two-dimensional colloidal crystal template β-PbO₂ micron-layers

A β-PbO₂ micron-layer of suitable thickness was deposited on the two-dimensional colloidal crystal template of the stainless-steel substrate by the anodic oxidation method, as shown in Figure 3b. The stainless-steel substrate two-dimensional colloidal crystal template was used as the anode, and the

stainless-steel substrate was used as the cathode with an average current density of 5 mA·cm^{-2}, bath temperature of 40°C, and electrodeposition time of 11 minutes.

2.1.3 Preparation of stainless-steel substrate two-dimensional β-PbO$_2$ macroporous array layers

The stainless-steel substrate two-dimensional colloidal crystal template β-PbO$_2$ micron-layer was placed in a beaker containing an appropriate amount of methylbenzene for ultrasonic treatment for 3 minutes, and then, the PS microspheres were dissolved and removed. After cleaning and drying, the stainless-steel substrate two-dimensional β-PbO$_2$ macroporous array layer was preliminarily obtained, as shown in Figure 3c.

2.1.4 Preparation of 2D-PbO$_2$ electrodes

The 2D-PbO$_2$ electrodes were obtained by redeposition of β-PbO$_2$ on a stainless-steel substrate two-dimensional β-PbO$_2$ macroporous array layer by the oxidation method, as shown in Figure 3d. The anode was the material prepared in *2.1.3*, and the cathode was a stainless-steel substrate. The average current density was 5 mA·cm^{-2} with a bath temperature of 40°C and electrodeposition time of 5 minutes.

2.2 Physicochemical characterization

The surface morphology of the 2D-PbO$_2$ electrodes and Flat-PbO$_2$ electrodes was studied by scanning electron microscopy (SEM, System Voltage 30 KV, XL30ESES-TM). The structure of the electrodes was characterized by X-ray diffraction (XRD, scan range 20-80, Xpert Powder) using Cu K$_\alpha$ radiation.

2.3 Electrochemical measurements

All the electrochemical measurements were performed on a CHI 660D electrochemical workstation (CHI600D, Shanghai Chenhua) with a three-electrode system. The three-electrode system used 2D-PbO$_2$ electrodes and Flat-PbO$_2$ electrodes (10 mm×10 mm) as the working electrode, a saturated calomel electrode (SCE) as the reference electrode and a platinum sheet (10 mm×10 mm) as the counter electrode.

All electrochemical measurements were conducted in a 0.05 mol·L^{-1} Na$_2$SO$_4$ solution at 25°C. The anode polarization curves were recorded under a sweep rate of 10 mV·s^{-1} between 1.0 V and 1.8 V (vs. SCE) to obtain the apparent activation energy (E_a), and linear sweep voltammograms at different temperatures (20-40°C) were measured. The cyclic voltammetry curves were recorded between 20 mV·s^{-1} and 100 mV·s^{-1} to calculate the double layer capacity value (C_{dl}) of the 2D-PbO$_2$ electrodes and Flat-PbO$_2$ electrodes. The frequency range of the EIS measurements was from 10 mHz to 100 KHz, and the measured potential voltage corresponded to a current density of 0.0025 A.

2.4 Electrochemical degradation of MO

2.4.1 Electrocatalytic degradation behavior of MO

All electrochemical measurements were conducted in 0.05 mol·L^{-1} Na$_2$SO$_4$ solution with and without 10.0 mg·L^{-1} MO at 25°C. The cyclic voltammetry curves were measured with a sweep rate of 10 mV·s^{-1} between 0.0 V and 1.8 V (vs. SCE) to obtain the degradation behavior.

Respectively, UV-vis diffuse reflectance spectroscopy was performed to determine the band gap energy of MO in the wavelength range of 200-600 nm using a Hitachi U-3010 spectrophotometer, where pure powdered Al$_2$O$_3$ was used as a reference sample.

2.4.2 Efficient electrochemical degradation of MO

The degradation of MO was carried out using 2D-PbO$_2$ electrodes and Flat-PbO$_2$ electrodes as the anodes and stainless steel as the cathodes with a working area of 8 cm^2 and an electrode distance of 3 cm. A 200 mL sample of 100.0 mg·L^{-1} MO in 0.1 mol·L^{-1} Na$_2$SO$_4$ was degraded in the cell. The average current density was controlled to be constant at 50 mA·cm^{-2} by a direct current potentiostat. The temperature was maintained at 25°C, the initial pH was 7, the magnetic stirring rate was 600 rpm, and the time was 180 minutes. A 722G UV-visible spectrophotometer was used to characterize MO at different electrolytic times at 464 nm.

3. RESULTS AND DISCUSSION

3.1 Physical characterization

3.1.1 Surface morphology analysis by SEM
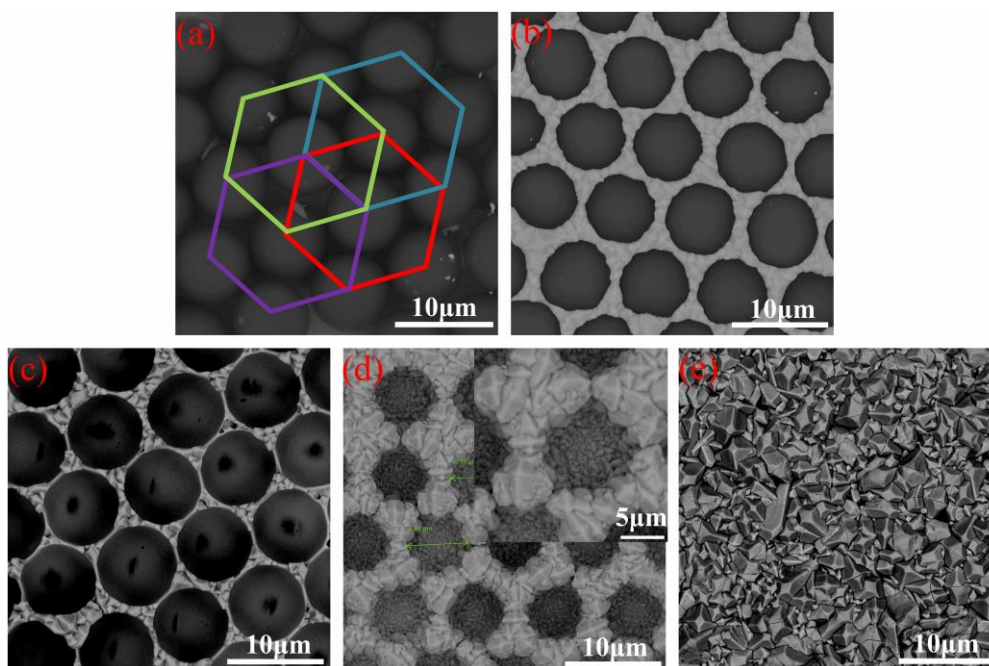
Figure 3. SEM images of the 2D-PbO$_2$ electrodes and Flat-PbO$_2$ electrodes (8000x). (a) Stainless-steel substrate two-dimensional colloidal crystal template (b) Stainless-steel substrate two-dimensional colloidal crystal template β-PbO$_2$ micron-layer;(c) Removal of PS microspheres; (d) 2D-PbO$_2$ electrodes; (e) Flat-PbO$_2$ electrodes.

Figures 3a-3d show the SEM images at 8000x magnification of the 2D-PbO₂ electrode fabrication process. In the process of preparing 2D-PbO₂ electrodes, because PS microspheres do not conduct electricity, the deposition of PbO₂ based on the two-dimensional colloidal crystal template of the stainless-steel substrate can only rely on the regular arrangement of the PS microsphere array, and the electric sediment β-PbO₂ grows along the gap between PS microspheres. After the first step was deposited on the template for 11 minutes, the PS microspheres were removed, and the β-PbO₂ micron active layer of the two-dimensional macropore with the stainless-steel substrate as the cavity bottom was preliminarily obtained, providing nucleation sites for the secondary deposition of PbO₂. Then, in the second step of deposition, the bottom of the macroporous cavity began to nucleate. The crystal grains were fine and uniform, and the microporous edges continued to grow on the crystal nucleus to form a typical tetragonal rutile structure of β-PbO₂ grains.

The SEM morphology of the 2D-PbO₂ electrodes and Flat-PbO₂ electrodes is shown in Figures 3d-3e. The 2D-PbO₂ electrodes exhibit two-dimensional macroporous array structures, which are independent and evenly distributed, and the channels are parallel to each other and perpendicular to the substrate surface. The average diameter of a single PbO₂ micron spherical cavity is approximately 6-7 μm, and the spacing of the micron holes is approximately 2 μm. Obviously, compared with the Flat-PbO₂ electrodes, the 2D-PbO₂ electrodes have a larger specific surface area and more active sites, indicating that the electrodes have the physical microstructure characteristics of high electrocatalytic activity[24].

3.1.2 Structure analysis by XRD
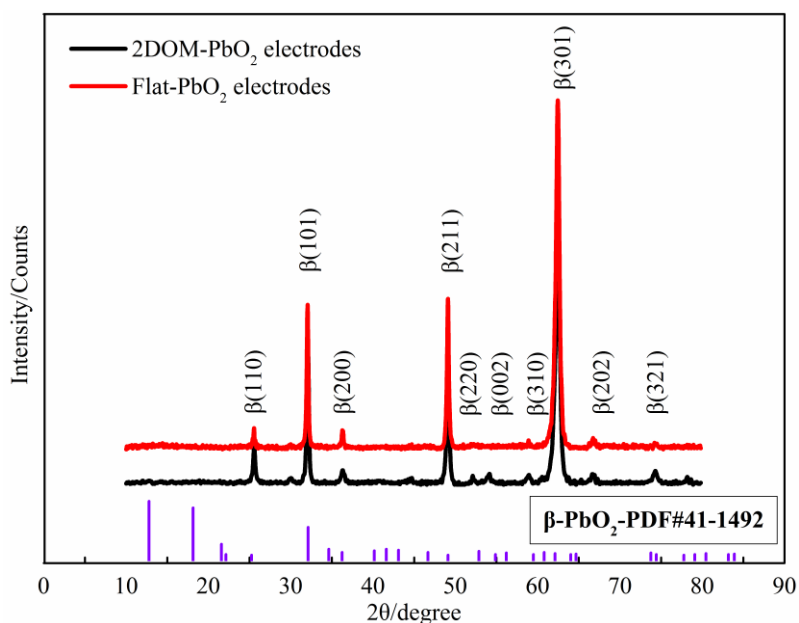
Figure 4. XRD pattern of 2D-PbO₂ electrodes and Flat-PbO₂ electrodes.

Figure 4 presents the XRD pattern of the 2D-PbO₂ electrodes and the Flat-PbO₂ electrodes. The diffraction peaks observed at 2θ=25.4°, 32.0°, 36.2°, 52.1°, 54.1°, 58.9°, 62.5°, 66.8° and 74.4° are assigned to the (110), (101), (200), (211), (220), (002), (310), (301), (202) and (321) planes, respectively, of β-PbO₂, which is in good agreement with the standard data of JCPDS card (number:

PDF#411492). According to the (301) diffraction peak half height and width, the average crystallite size (*D*) is calculated using Scherrer's formula as[24-26]：

$$D = \frac{K\lambda}{\beta \cos\theta}$$
(1)

where λ is the wavelength of Cu K_α radiation (λ=1.5418 Å), β is the corrected half width of the diffraction peak, θ is the diffraction angle, and *K* is a constant equal to 0.9. The average grain sizes of the 2D-PbO$_2$ electrodes and Flat-PbO$_2$ electrodes are calculated by the Scherrer equation. The crystallite size of the 2D-PbO$_2$ electrodes is 128 Å, which is far smaller than that of Flat-PbO$_2$ electrodes, 199 Å. Thus, the particle size of the 2D-PbO$_2$ electrodes is significantly reduced, which is conducive to the formation of a large specific surface area and more active sites. This is consistent with the SEM results.

3.2 Performance analysis of electrocatalytic degradation

3.2.1 Anodic polarization curves—Tafel characterization
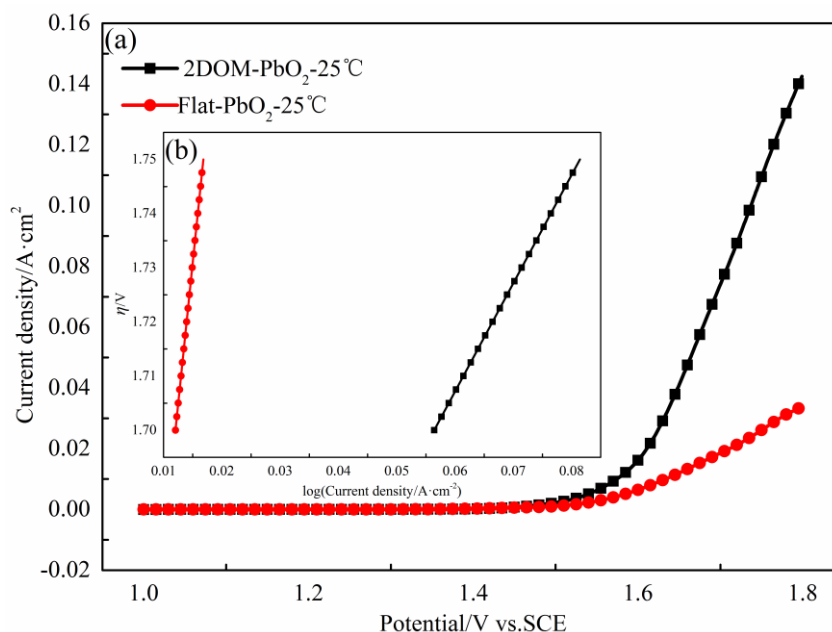
Figure 5. Anode polarization curves of the 2D-PbO$_2$ electrodes and Flat-PbO$_2$ electrodes in 0.05 mol·L^{-1} Na$_2$SO$_4$ (a); Tafel linear fitting curves (b).

To reduce the influence of the solution resistance on the reaction, the anode polarization curves for the Tafel analysis were corrected using formula (2)[27-28] to present the real potential value of the electrocatalytic reaction:

$$E_c = E_{appl} - iR_s$$
(2)

where E_c is the corrected potential, E_{appl} is the applied potential, *i* is the faradaic current and R_s is the uncompensated electrolyte resistance. Figure 5a shows the iR_s-corrected anode polarization curves of the 2D-PbO$_2$ electrodes and Flat-PbO$_2$ electrodes in 0.05 mol·L^{-1} Na$_2$SO$_4$. Figure 5b shows the iR_s-corrected Tafel lines (η-log*i*)[27-31]:

$$\eta = a + b\log i$$
(3)

where η and i represent the overpotential of oxygen evolution and the faradaic current, respectively.

The oxygen evolution kinetic parameters of the 2D-PbO$_2$ electrodes and Flat-PbO$_2$ electrodes are shown in Table I, where a and b are the constants obtained through linear fitting of the relationship of η and $logi$ in Origin software. When the overpotential of oxygen evolution $\eta=0$[28-31], the electrode surface exchange current density j^0 can be calculated using the Tafel formula (4).

$$\eta = E_c + 0.231V - 0.8025V \tag{4}$$

where E_c (SCE) is the corrected potential, 0.231 V (NHE) is the potential of the SCE, and 0.8025 V is the reversible potential of oxygen evolution calculated from the Nernst equation using 0.05 mol·L^{-1} Na$_2$SO$_4$ at 25°C.

Table I. Oxygen evolution kinetic parameters of the 2D-PbO$_2$ electrodes and Flat-PbO$_2$ electrodes.

Electrode	E_c (V)	a (V)	b (V·dec^{-1})	j^0 (A·cm^{-2})	η (V)
2D-PbO$_2$	1.556	1.520	0.315	1.478×10^{-5}	0.9845
Flat-PbO$_2$	1.583	1.788	0.344	6.428×10^{-6}	1.0115

The overpotentials values η are identified as one of the most important criteria for an electrocatalytic reaction, and the Tafel intercept a represents the overpotential value when the current density is 1 A·cm^{-2}. When the value of a is large, the cell voltage during electrolysis and the power consumption will be greater. As shown in Table I, compared with the η of the Flat-PbO$_2$ electrodes in 0.05 mol·L^{-1} Na$_2$SO$_4$, the potential value of 2D-PbO$_2$ electrodes is reduced by 27.0 mV, a decreased of 0.268 V. This difference indicates that the oxygen evolution reaction of the 2D-PbO$_2$ electrodes has less resistance, the reaction rate is faster, and the reaction energy consumption is small.

When the electrode is in a stable oxygen evolution zone, the j^0 of the 2D-PbO$_2$ electrodes is 1.47797×10^{-5} A·cm^{-2}, which is an order of magnitude higher than that of the Flat-PbO$_2$ electrodes, indicating[24] that the 2D-PbO$_2$ electrodes react at a high rate, the reversibility is also high, and the depolarization is strong. In other words, the 2D-PbO$_2$ electrode system is not easily polarized, more easily reacts, and has a better electrocatalytic performance. Obviously, the 2D-PbO$_2$ electrodes have a smaller oxygen evolution potential and larger exchange current density than the flat electrodes, so the reaction requires less energy, making the reaction easier to perform and reducing energy consumption, resulting in excellent oxygen evolution electrocatalytic performance.

3.2.2 Anodic polarization curves—Apparent activation energy, E_a
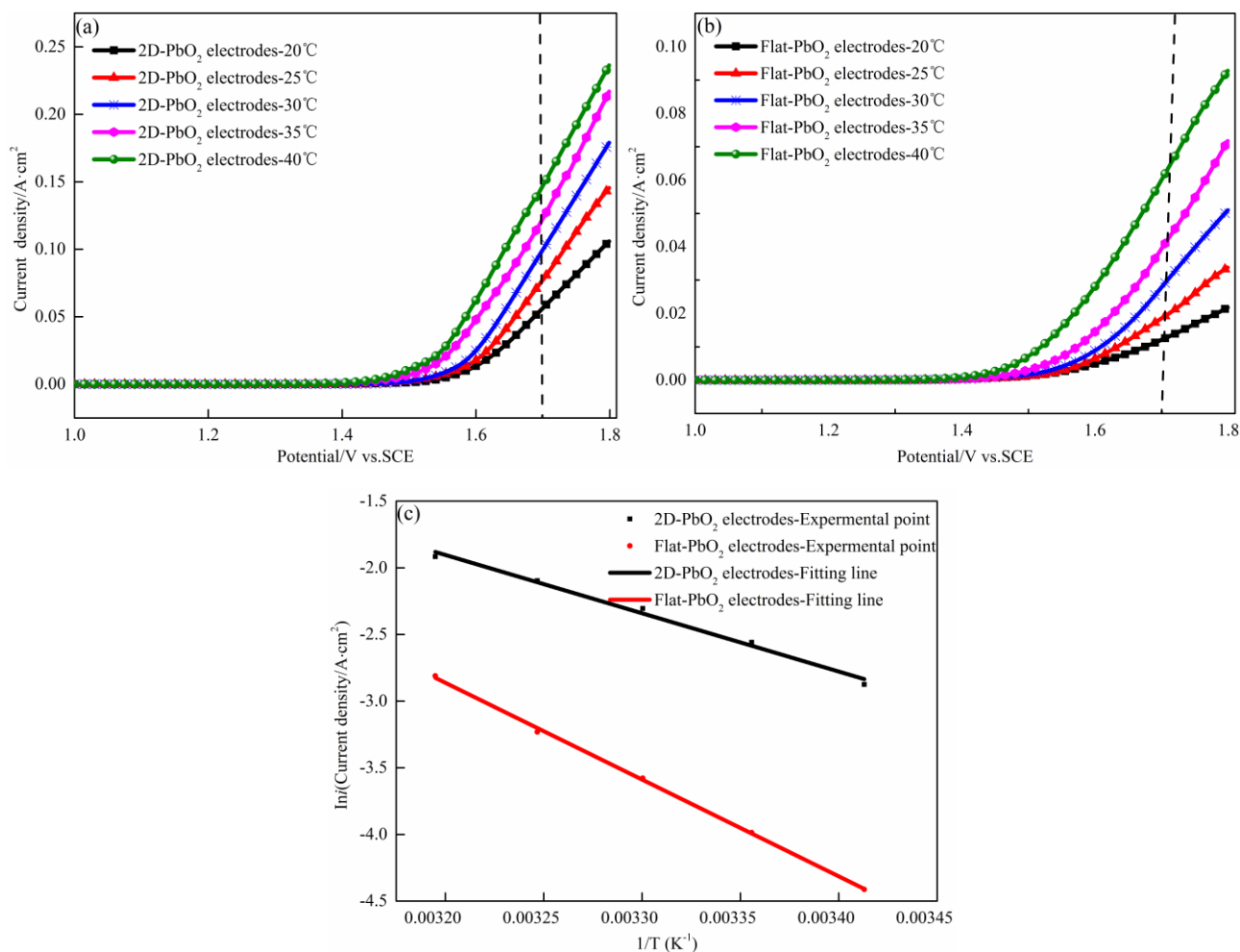
Figure 6. Anode polarization curves of 2D-PbO$_2$ electrodes (a) and Flat-PbO$_2$ electrodes (b) at different electrolyte temperatures in 0.05 mol·L^{-1} Na$_2$SO$_4$; *lni-T^{-1}* linear fitting curves (c).

Table II. The apparent activation energy E_a of the 2D-PbO$_2$ electrodes and Flat-PbO$_2$ electrodes.

Electrode	E_a (kJ·mol^{-1})
2D-PbO$_2$	12.09
Flat-PbO$_2$	20.37

It is known that whether a reaction occurs easily or cannot be characterized by the apparent activation energy. Lowering the apparent activation energy is the common feature of a catalytic reaction. The smaller the activation energy is, the better the electrocatalytic performance of the electrode and the easier the degradation reaction. By plotting the working electrode anodic polarization curve at different temperatures (*T*), the apparent activation energy (E_a) can be determined using the Arrhenius law[32]:

$$\ln i = \ln A - \frac{E_a}{RT} \tag{5}$$

where A is the pre-exponential factor, R is the gas constant (8.314 J·mol^{-1}·K^{-1}), T is the absolute temperature, and E_a is the molar activation energy.

The anodic polarization curve between 20°C and 45°C of the 2D-PbO$_2$ electrodes and Flat-PbO$_2$ electrodes in 0.05 mol·L^{-1} Na$_2$SO$_4$ are shown in Figures 6a and 6b. The current density corresponding to the oxygen evolution potential in the stable oxygen evolution zone is taken as i, and the chart of lni-T^{-1} can be plotted (Figure 6c). The activation energy can be calculated from the slope of the straight line and is listed in Table II. The activation energy of the Flat-PbO$_2$ electrodes is 20.37 kJ·mol^{-1}, and the activation energy of the 2D-PbO$_2$ electrodes is 12.09 kJ·mol^{-1}, indicating that the 2D-PbO$_2$ electrodes have a smaller energy barrier, which is consistent with the conclusion from the Tafel analysis of the anode polarization curve. The main reasons for this result may be as follows. The 2D-PbO$_2$ electrodes have the structure of a two-dimensional macroporous array, the grain size of the sedimentary layer is fine and uniform, the specific surface area is larger, and the active material of the electrode active layer that can be used in the electrocatalytic reaction process increased, accelerating the reaction rate, which is reflected in the improvement in the electrocatalytic performance.

3.2.3 Cyclic voltammetry curves—Electric double layer capacitance, C_{dl}
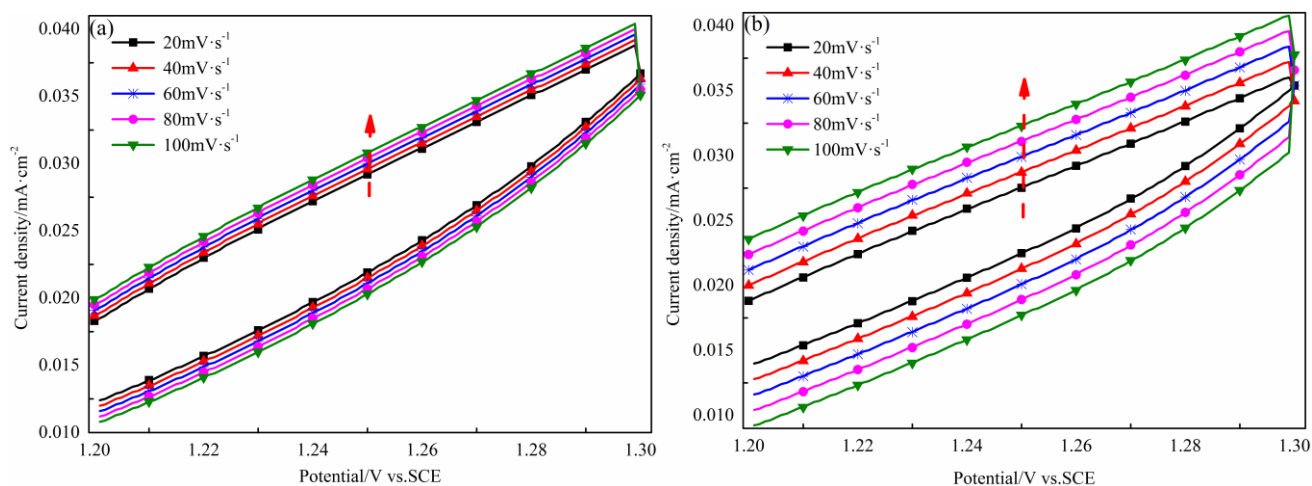
Figure 7. Voltammetric curves of the 2D-PbO$_2$ electrodes (a) and Flat-PbO$_2$ electrodes (b) at different scan rates in the capacitive potential region (1.2-1.3 V).

Table III. The electric double layer capacitance C_{dl} of the 2D-PbO$_2$ electrodes and Flat-PbO$_2$ electrodes.

Electrode	2D-PbO$_2$	Flat-PbO$_2$
C_{dl} (µF·cm^{-2})	60.00	20.00

A large number of studies have shown that the electrocatalytic degradation activity of oxide active anodes depends not only on the characteristics of the material itself but also on the amount of

active sites on the electrochemically active surface[28]. However, the active surface area can be evaluated using the electric double layer capacitance C_{dl} (1.1-1.4 V), which only occurs in the double-layer of a nonfaradaic charging process.
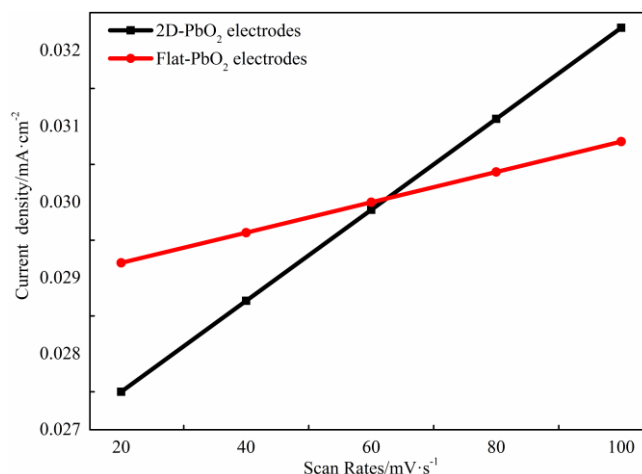
Figure 8. Plots of the current density at 1.25 V vs. the scan rate.

To further study the amount of coating surface active sites for the electrocatalytic reaction, a narrow potential double capacitive potential area was selected, and cyclic voltammograms were obtained at different scan rates. As shown in Figure 7, all electrode voltammetric curves were recorded between 1.2 V and 1.3 V as a function of the scan rate, v (20<100 mV·s^{-1}), and the current was measured, i_E, at a constant potential (E=1.25 V). The potential used to measure the current is located in a region of the voltammetric curve where the redox transitions are minimized. The double-layer capacitance is obtained from the slope i_E vs. v graphs and is shown in Figure 8. As shown in Table III, the double-layer capacitance values of the Flat-PbO$_2$ electrodes and 2D-PbO$_2$ electrodes are 20 μF·cm^{-2} and 60 μF·cm^{-2}, respectively, which indicates the 2D-PbO$_2$ electrodes have three times the surface active sites of the Flat-PbO$_2$ electrodes. This is due to the two-dimensional macroporous array structure of the 2D-PbO$_2$ electrodes, which changes the double-layer structure of the electrode. The fine-grained grains in the macroporous cavity of the 2D-PbO$_2$ electrodes are uniform, and the grains at the edge of the cavity are dense, which increases the specific surface area of the coating to affect the capacitance of the electric double layer. The results shows that the specific surface area of the 2D-PbO$_2$ electrodes obviously improved, and the number of surface active sites increased, thus indirectly increasing the electrochemical catalytic activity area, which is also the cause of the increase in the electric double layer capacitance; the electrocatalytic activity of the electrode also improved[25].

3.2.4 Electrochemical impedance spectroscopy—Charge transfer resistance, R_{ct}
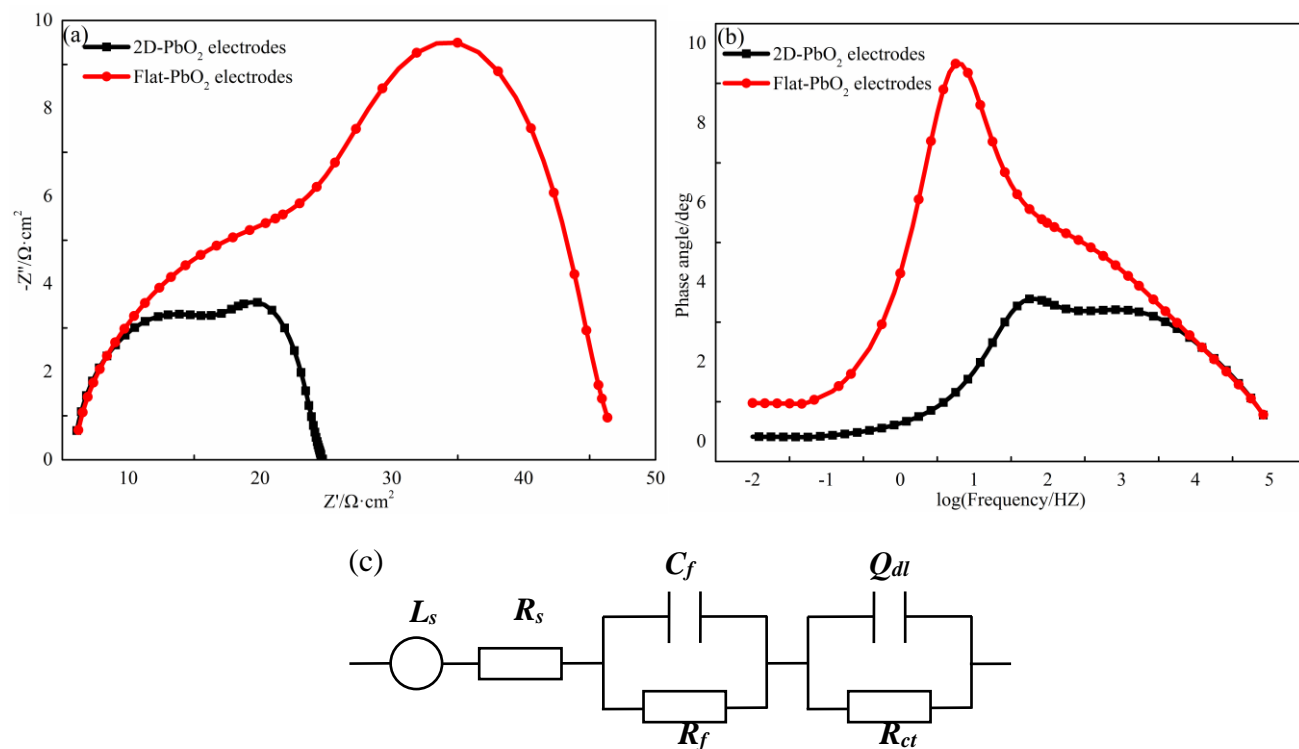
Figure 9. EIS of 2D-PbO$_2$ electrodes and Flat-PbO$_2$ electrodes in 0.05 mol·L^{-1} Na$_2$SO Nyquist diagrams (a), Bode plots (b) and equivalent circuit $LR_s(R_fC_f)(R_{ct}Q_{dl})$ (c).

Table IV. The parameters obtained by simulation with the equivalent circuit model $LR_s(R_fC_f)(R_{ct}Q_{dl})$ according to the EIS spectra shown in Figure 9.

Electrode	L (Henri·cm^{-2})	R_s (Ω·cm^2)	C_f (F·cm^2)	R_f (Ω·cm^2)	Q_{dl} (S·s^n·cm^{-2})	n	R_{ct} (Ω·cm^2)
2D-PbO$_2$	1.389×10^{-6}	4.194	9.900×10^{-4}	3.65	9.033×10^{-3}	0.459	16.89
Flat-PbO$_2$	1.333×10^{-6}	4.045	2.310×10^{-3}	12.68	2.217×10^{-3}	0.387	30.84

Electrochemical impedance spectroscopy (EIS), a powerful technique for analyzing the interfacial characteristics of an electrode, was used to study the electrocatalytic degradation performance of the 2D-PbO$_2$ electrodes and Flat-PbO$_2$ electrodes in 0.05 mol·L^{-1}Na$_2$SO$_4$. The Nyquist diagrams, Bode plots and equivalent circuit model for the 2D-PbO$_2$ electrodes and Flat-PbO$_2$ electrodes are presented in Figure 9. In the Nyquist complex plan, the entire frequency domain shows an inductance arc and capacitance arc, the inductance arc in the high-frequency region corresponds to the physical response of the macropore array structure on the electrode active layer, and the other arc in the low-frequency domain of the complex plane is attributed to the electrochemical reaction at the interface between the active oxide layer and the solution. Similarly, it is obvious from the Bode plots

that there are two phase angular peaks in the low-frequency and high-frequency domains, corresponding to the two capacitance arcs and two time constants in the Nyquist diagrams.

The equivalent circuit (EEC) can be characterized as $LR_s(R_fC_f)(R_{ct}Q_{dl})$[28, 33, 34], as shown in Figure 9c. The EEC has often been used to simulate the impedance data for the electrocatalytic reaction process of an oxide electrode in previous literature. An excellent adjustment ($x^2 < 10^{-4}$) was obtained, indicating that the selected equivalent circuit can better reflect the oxygen evolution reaction behavior of the prepared electrode in a 0.05 mol·L^{-1} Na$_2$SO$_4$ solution. In the equivalent circuit, R_s stands for the uncompensated solution resistance. The reason for the formation of L is that the tip of the Lujin capillary is too close to the working electrode to create a shielding effect. R_f is the resistance of the oxide layer, and C_f is the corresponding capacitance. The (R_fC_f) combination is connected with the physical response of the macropore array structure of the electrodes observed in the intermediate and high-frequency domains. R_{ct} is the charge transfer resistance for the oxygen evolution reaction, and C_{dl} is the corresponding capacitance. The ($R_{ct}C_{ct}$) combination is definitely related to the process of the oxygen evolution reaction in the low-frequency arc. Taking the nonhomogeneity of the electrode surface into consideration, a constant phase element (*CPE*) is applied to replace the capacitive element. The impedance of the *CPE* can be represented as[27, 34]:

$$Z_{CPE} = \frac{1}{Q(jw)^n} \tag{6}$$

where Q is the *CPE* constant, n is the *CPE* power and w is the angular frequency.

As shown in Table IV, it is clear that the values of L and R_s change little, suggesting that the experimental research states of the two electrodes are basically the same. Previous studies[24, 25, 28, 33, 34] suggested that Q_{dl} and R_{ct} can reliably evaluate and explain the electrocatalytic degradation activity of electrodes. The larger values of Q_{dl} and smaller values of R_{ct} are thought to be more conducive to a catalytic reaction, which indicates that the electrode has better electrocatalytic degradation activity. The R_{ct} value and C_{dl} value of the 2D-PbO$_2$ electrodes are 16.890 Ω·cm^2 and 9.033×10^{-3} S·s^n·cm^{-2}, respectively, while the R_{ct} value and C_{dl} value of the Flat-PbO$_2$ electrodes are 30.840 Ω·cm^2 and 2.217×10^{-3} S·s^n·cm^{-2}, respectively. The 2D-PbO$_2$ electrodes have smaller charge transfer resistance R_{ct} and larger double-layer capacitance C_{dl} values than the Flat-PbO$_2$ electrodes, so the resistance of the charge transfer process is smaller and the oxygen evolution reaction is easier. This indicates that the two-dimensional macroporous array structure reduces the charge transfer resistance of the 2D-PbO$_2$ electrodes, effectively improves the electron transfer rate and improves the electrocatalytic degradation performance of the electrode for organic pollutants[24].

3.3 Electrocatalytic degradation of MO

3.3.1 Electrocatalytic degradation behavior of MO

To investigate the electrocatalytic degradation behavior of MO with the 2D-PbO$_2$ electrodes, cyclic voltammograms were obtained in a 0.05 mol·L^{-1} Na$_2$SO$_4$ solution with and without 10.0 mg·L^{-1} MO at a scan rate of 10 mV·s^{-1} at 25°C, as shown in Figure 10.

When the potential was from 0.0 V to 1.8 V in the forward scan, a significant oxidation peak (AB segment) appeared near 1.35-1.45 V in the 10.0 mg·L^{-1} MO solution. Compared with the CV curve in a 0.05 mol·L^{-1} Na$_2$SO$_4$ blank solution, the electrochemical reaction in this potential area was related to the electrochemical oxidation of MO on the electrode surface, corresponding to the electrocatalytic degradation of MO. Its anode peak I_p current increased to 0.005 A·cm^{-2}, implying that the oxidation process was caused by direct electrochemical oxidation[24, 35, 36].
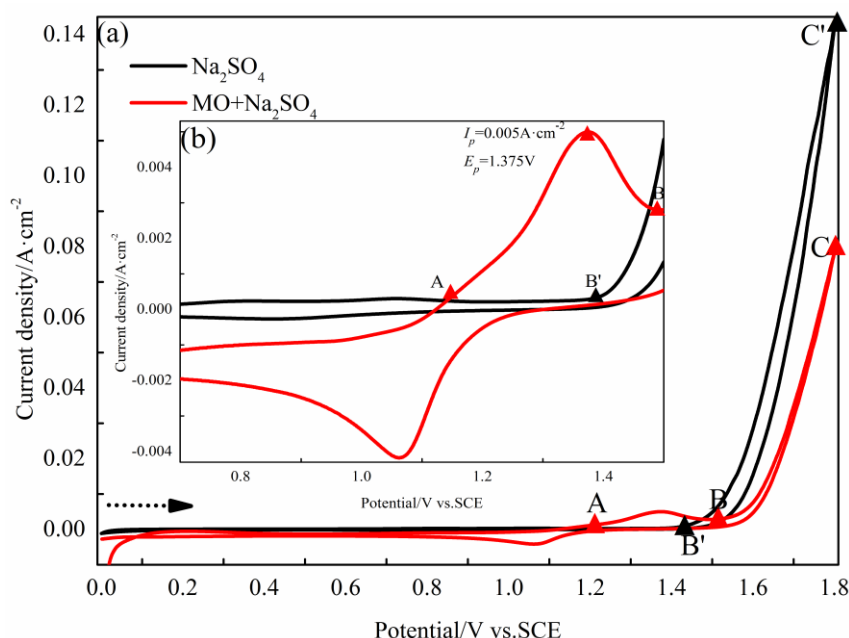
Figure 10. Cyclic voltammetry curves of the 2D-PbO$_2$ electrodes and Flat-PbO$_2$ electrodes in 0.05 mol·L^{-1} Na$_2$SO$_4$ without and with 10.0 mg·L^{-1} MO at 25°C and a scan rate of 10 mV·s^{-1}.

In fact, the electrochemical oxidation of MO is achieved by the reaction of β-PbO$_2$ with •OH adsorbed at the active site on the electrode surface to form a high-value oxide (PbO_{2+x}), which is then degraded by the redox reaction with MO. Moreover, many researchers have identified the degradation behavior of organic pollutants on inactive electrodes (MO_x), such as PbO$_2$ and SnO$_2$[8, 32, 37]. In the first stage, H_2O discharges from the anode to form the adsorbed hydroxyl radical (•OH) (equation 7), which is then adsorbed on the active site of the electrode (equation 8):

$$H_2O \rightarrow \cdot OH + H^+ + e^- \tag{7}$$

$$MO_x + \cdot OH \rightarrow MO_x(\cdot OH) + H^+ + e^- \tag{8}$$

In the second stage, MO_x reacts with •OH to form high-value oxide MO_{x+1} (equation 9), which then reacts with organic pollutant R for degradation (equation 10):

$$MO_x(\cdot OH) \rightarrow MO_{x+1} + H^+ + e^- \tag{9}$$

$$MO_{x+1} + R \rightarrow MO_x + RO \tag{10}$$

At the same time, the oxygen evolution reaction occurs due to the chemical decomposition of MO_{x+1}, which will compete with the degradation reaction (equation 11):

$$MO_{x+1} \rightarrow MO_x + \frac{1}{2}O_2 \tag{11}$$

As shown in Figure 10a, as the potential continued to increase, the 2D-PbO$_2$ electrodes in 0.05 mol·L^{-1} Na$_2$SO$_4$ had a stable oxygen evolution interval (B'C' segment) of 1.5-1.8 V, and the 0.05 mol·L^{-1} Na$_2$SO$_4$ with 10.0 mg·L^{-1}MO oxygen evolution interval (BC segment) moved to 1.7-1.8 V, which indicated that PbO_{2+x} preferentially reacts with MO in the presence of 10.0 mg·L^{-1}MO in sodium sulfate solution (equation 10), consuming a large amount of strongly oxidizing •OH [24, 36, 37, 38] on the surface of the electrode and inhibiting the occurrence of competitive side reactions (equation 11), thus leading to oxygen evolution. Therefore, this leads to a decrease in the power loss to oxygen generation and improves the current efficiency for the electrochemical degradation of MO.
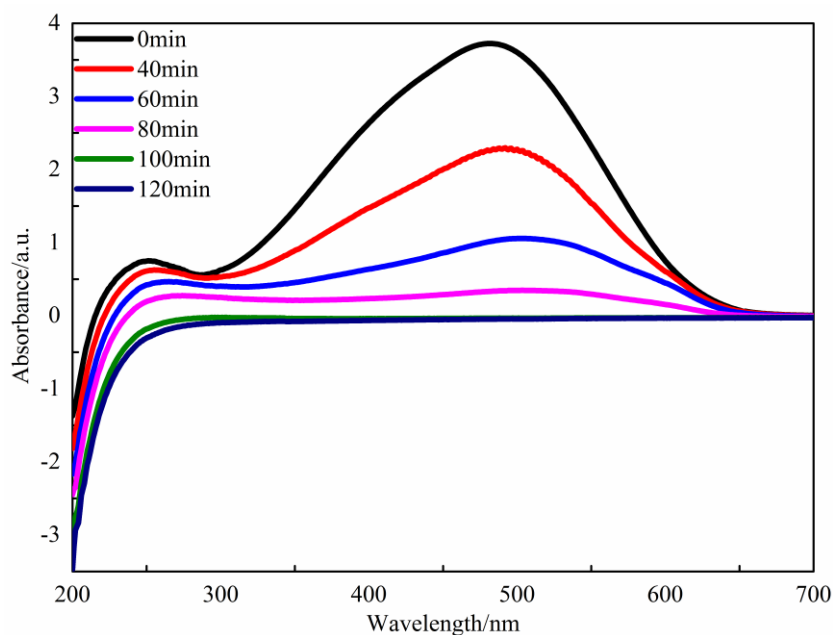
Figure 11. UV-absorption spectra of the MO degradation solution at different electrolysis times (0 minutes to 120 minutes).

To examine the kinetics of MO decolorization and the types and amounts of intermediate products of decomposition[36], UV-vis spectroscopy was used to monitor the changes in the absence of MO aqueous solution as a function of time. The UV spectrum of MO before treatment presented two defined absorption bands, with an obvious peak observed at 271 nm assigned to the aromatic rings in the MO molecules and another characteristic peak at 464 nm attributed to the conjugated structure constructed via the azo backbone (-N=N-) of MO[35, 39-42]. It can be observed that the concentration of MO decreases gradually as a function of irradiation time under UV-light irradiation, and the peak (A=464 nm) nearly disappears after 100 minutes, further confirming that the electrocatalytic degradation of MO is basically complete. It has been speculated[35, 36, 43] that the degradation

pathway of MO is the cleavage of azo bonds, which may form the intermediates N,n-dimethyl p-phenylenediamine and sulfonic acid.
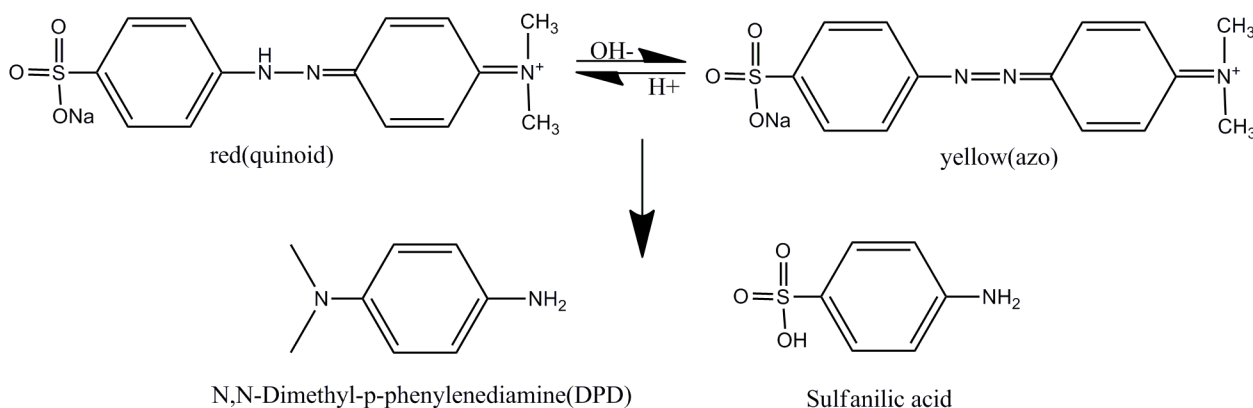
Figure 12. Proposed structures of the main intermediates of MO dye degradation.

3.3.2 Efficient electrochemical degradation of MO
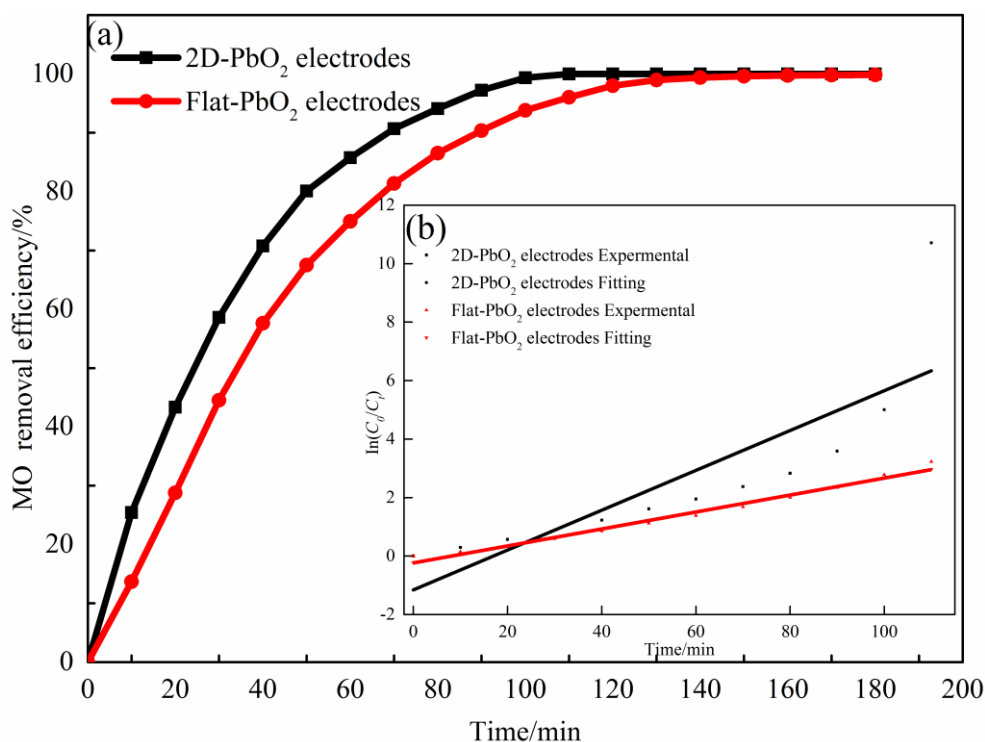
Figure 13. MO removal efficiency of 2D-PbO$_2$ electrodes and Flat-PbO$_2$ electrodes over time (a); Kinetics of MO electrochemical degradation on the electrodes (b) (initial pH=7, T=25°C, current density=50 mA·cm^{-2}, initial concentration of MO=100.0 mg·L^{-1}, concentration of supporting electrolyte Na$_2$SO$_4$=0.1 mg·L^{-1}).

Table V. The pseudofirst-order reaction kinetic parameters of the MO degradation process.

Electrode	Fitting equation	$K_{app} \times 10^{-3}$ (min^{-1})	R^2
2D-PbO$_2$	ln(C_o/C_t)=0.06814t-1.1607	68.14	0.99181
Flat-PbO$_2$	ln(C_o/C_t)=0.02902t-0.2234	29.02	0.98206

Table VI. Removal efficiency for MO degradation on different electrodes

Electrode	Removal efficiency (%)	Pollutant and degradation conditions	Ref
TiRuSnO$_2$ (DSA) (50 cm^2)	69.00	MO 100.0 mg·L^{-1}, Na$_2$SO$_4$ 0.5 mol·L^{-1}, 50A, T=25°C, flow rate: 300 L·h^{-1}, 3 h	[8]
Ti/Ce-nanoTiO$_2$/Ce-PbO$_2$ (8.3 cm^2)	99.60	MO 100.0 mg·L^{-1}, Na$_2$SO$_4$ 0.05 mol·L^{-1}, 50 mA·cm^{-2}, pH=5, at the temperature, 120 min	[24]
porous-Ti/SnO$_2$-Sb (3 cm^2)	92.00	MO 100.0 mg·L^{-1}, Na$_2$SO$_4$ 1.0 mol·L^{-1}, 120 min	[44]
BBD (3 cm^2)	Almost completely removed	MO 50.0 mg·L^{-1}, Na$_2$SO$_4$ 0.1 mol·L^{-1}, 50 mA·cm^{-2}, pH=6, 90 min	[45]
Flat-PbO$_2$ (8 cm^2)	74.94	MO 100.0 mg·L^{-1}, Na$_2$SO$_4$ 0.1 mol·L^{-1}, 50 mA·cm^{-2}, pH=7, T=25°C, 60 min	This work
2D-PbO$_2$ (8 cm^2)	90.69/100	MO 100.0 mg·L^{-1}, Na$_2$SO$_4$ 0.1 mol·L^{-1}, 50 mA·cm^{-2}, pH=7, T=25°C, 60 min/100 min	This work

For applications removing organic pollutants, it is important to investigate the electrocatalytic degradation efficiency of the 2D-PbO$_2$ electrodes and Flat-PbO$_2$ electrodes. As shown in Figure 13a, the MO removal efficiency increases with time. With the extension of the degradation time, the removal amounts of both electrodes increased. After 60 minutes, the degradation efficiency of the original pollutants with the 2D-PbO$_2$ electrodes and Flat-PbO$_2$ electrodes was 90.69% and 74.94%, respectively, and the 2D-PbO$_2$ electrodes reached 100% after 100 minutes. For comparison, Table VI gives the MO removal efficiency obtained on the 2D-PbO$_2$ electrodes, Flat-PbO$_2$ electrodes and on other types of electrodes reported in the literature [8, 24, 44, 45]. The 2D-PbO$_2$ electrodes prepared in this work could degrade pollutants more effectively than other electrodes under similar conditions, and the 2D-PbO$_2$ electrodes have good activity.

It was reported that the decolorization of MO can be described as pseudo first-order kinetics. The Langmuir–Hinshelwood pseudo first-order kinetic model can be expressed by the following formula[36, 37, 41]:

$$\ln(\frac{c_0}{c_t})=k_{app}t \tag{12}$$

where c_t is the concentration of the reactant at t time, c_0 is the initial concentration of the reactant and k_{app} is the reaction apparent rate constant. As shown in Figure 14b and Table V, the values of k_{app} could be obtained from the linear fitting of the curves of $ln(c_0/c_t)$ vs. t. The reaction apparent rate constant (k_{app}) value at the 2D-PbO$_2$ electrodes was 0.06814 min^{-1}, which was approximately 2.35 times higher than that on Flat-PbO$_2$ electrodes (0.02909 min^{-1}). The electrocatalytic degradation of MO with a 2D-PbO$_2$ electrode is more efficient and has excellent electrocatalytic degradation performance.

4. CONCLUSION

In summary, two-dimensional β-PbO$_2$ macroporous array electrodes were fabricated for electrocatalytic degradation of MO. Compared with the Flat-PbO$_2$ electrodes, the 2D-PbO$_2$ electrodes have better electrocatalytic degradation performance and higher efficiency for MO degradation, which can be attributed to the two-dimensional macroporous array structure of the electrode.

1. Compared with Flat-PbO$_2$ electrodes, the two-dimensional macroporous inverse phase spherical cavity array structure of the 2D-PbO$_2$ electrodes has a larger specific surface area and more active sites; thus, the 2D-PbO$_2$ electrodes have a higher exchange current density, smaller apparent activation energy, larger electric double layer capacitance and smaller charge transfer resistance.

2. The electrocatalytic degradation of MO on the 2D-PbO$_2$ electrodes showed that the conjugated structure constructed via the azo backbone was cleaved by direct electrochemical oxidation. The electrocatalytic degradation reaction followed pseudo first-order kinetics, and the apparent rate constant (k_{app}) value was 0.06814 min^{-1}, which was 2.35 times greater than that of Flat-PbO$_2$ (0.02902 min^{-1}).

References

1. K. Piaskowski, R. Świderska-dąbrowska, and P. K. Zarzycki, *Journal of Aoac International*, 101 (2018) 1371.
2. Z. G. Aguilar, E. Brillas, M. Salazar, J. L. Nava, J. Sirés, *Applied Catalysis B Environmental*, 206 (2017) 44.
3. X. L. Tang, *Guangdong Chemical Industry*, 44 (2017) 208.
4. C. Y. Wang, F. W. Wang, M. Xu, C. G. Zhu,W. Y. Fang, Y. J. Wei, *Journal of Electroanalytical Chemistry*, 759 (2015) 158.
5. H. Xu, Q. Zhang, W. Yan, W. Chu, L. F. Zhang, *International Journal of Electrochemicalence*, 8 (2013) 5382.
6. W. L. Zhang, H. S. Kong, H. B. Lin, H. Y. Lu, W. M. Huanng, J. Yin, Z. Q. Lin, J. P. Bao, *Journal*

of Alloys and Compounds, 650 (2015) 705.

7. M. Xu, Y. L. Mao, W. L. Song, X. M. OuYang, Y. H. Hu, Y. J. Wei, C. G. Zhu, W. Y. Fang, B. C. Shan, R. Lu, F. W. Wang, *Journal of Electroanalytical Chemistry*, 823 (2018) 193.
8. L. Labiadh, A. Barbucci, M. P. Carpanese, A. Gadri, S. Ammar, M. Panizza, *Journal of Electroanalytical Chemistry*, 766 (2016) 94.
9. L. R. Hou, L. Lian, L. Zhou, L. H. Zhang, C. Z. Yuan, *Materials Research Bulletin*, 60 (2014) 1.
10. W. Yan, Z. Chen, Q. Yu, W.Zhu, H. Wang, and B. Q. Du, *Journal of The Electrochemical Society*, 163 (2016) D414.
11. A B Velichenko, D V Girenko, F I Danilov, *Journal of Electroanalytical Chemistry*, 405 (1996) 127.
12. V A Knysh, T. V. Luk'anenko, P. Y. Demchenko, R. Y. Gladyshevskii, and A. B. Velichenko, *Protection of metals and physical chemistry of surfaces*, 54 (2018) 1038.
13. M. L. Braunger, E. A. Silva, H. Awada, V. J. Oliveira, H. S. Silva, D. Bégué, R. C. Hiorns, *Polymer International*, 67 (2018) 1028.
14. J. Chowdhury, S. Saha, M. Ghosh, *Materials Today Proceedings*, 5 (2018) 10071.
15. N. A. Stepashkin, M. K. Chernenko, V. D. Khripun, N. S. Ivanov, N. G. Sukhodolov, *Thin Solid Films*, 661 (2018) 1.
16. S. Yang, S. G. Jang, D. Choi, S. Kim, and H. K. Yu, *Small*, 2 (2006) 458.
17. Z. Chen, P. Zhan, Z. L. Wang, J. H. Zhang, W. Y. Zhang, N. B. Minutesg, C. T. Chan, and P. Sheng, *Advanced Materials*, 16 (2004) 417.
18. P. Jiang, T. Prasad, M. J. Mcfarland, V. Lcolvin, *Applied Physics Letters*, 89 (2006) 011908-1.
19. M. Danno, S. Yoshinari, S. Igari, J. Honda, T. Eguchi, W. Inoue, K. Yasuhara, S. Hara, H. Ikake, S. Shimizu, T. Toyama, Y. Kusaka, N. Fukuda, H. Ushijima, K. Takase, K. Sugawa, and J. Otsuki, *Chemistry Letters*, 47 (2018) 429.
20. P. N. Bartlett, T. Dunford, and M. A. Ghanem, *Journal of Materials Chemistry*, 12 (2002) 3130.
21. P. Jiang, and M. J. Mcfarland, *Journal of the American Chemical Society*, 127 (2005) 3710.
22. X. Yan, J. Yao, X. Li, J. H. Zhang, K. Han, and B. Yang, *Journal of the American Chemical Society*, 127 (205) 7688.
23. R. Dommelen, P. Fanzio, L. Sasso, *Advances in Colloid and Interface Science*, 251 (2018) 97.
24. M. Xu, Z. C. Wang, F. W. Wang, P. Hong, C. Wang, X. M. Ouyang, C. G. Zhu, Y. J. Wei, Y. H. Hun, W. Y. Fang, *Electrochimica Acta*, 201 (2016):240-250.
25. Y. W. Yao, X. Chen, N. C. Yu, H. S. Dong, and H. R. Wang, *Journal of The Electrochemical Society*, 164 (2017) E48.
26. M. M. Islam, S. Basu, *Journal of Environmental Chemical Engineering*, 3(2015) 2323.
27. Y. Q. Lai, Y. Li, L. X. Jiang, W. Xu, X. J. Lv, J. Li, Y. X. Liu, *Journal of Electroanalytical Chemistry*, 671 (2012) 16.
28. H. X. Li, Z. Chen, Q. Yu, W. Zhu, and W. R. Cui, *Journal of The Electrochemical Society*, 164 (2017) H1064.
29. H. T. Yang, B. Chen, Z. C. Guo, H. R. Liu, Y. C. Zhang, H. Huang, R. D. Xu, R. C. Fu, *Transactions of Nonferrous Metals Society of China*, 24 (2014) 3394.
30. R. D. Xu, L. P. Huang, J. F. Zhou, P. Zhan,Y. Yguan, Y. Kong, *Hydrometallurgy*, 125 (2012) 8.
31. H. T. Yang, Buminutesg Chen, H. R. Liu, Z. C. Guo,Y. C. Zhang, X. L. Li, R. D. Xu, *International Journal of Hydrogen Energy*, 39 (2014) 3087.
32. Minutesghua Zhou, Qizhou Dai, Lecheng Lei, ChunAn Ma, and Dahui Wang, *Environmental Science and Technology*, 39 (2005) 363.
33. H. Z. Cao, D. H. Lu, J. P. Lin, Q. Ye, J. J. Wu,G. Q. Zheng, *Electrochimica Acta*, 91 (2013) 234.
34. Z. G. Ye, H. Meng, D. B. Sun, *Journal of Electroanalytical Chemistry*, 621 (2008) 49.
35. X. L. Li, X. Li, W. J. Yang, X. H. Chen, W. L. Li, B. Luo, K. L. Wang, *Electrochimica Acta*, 146 (2014) 15.
36. H. Yang, J. T. Liang, L. Zhang, Z. H. Liang, *International Journal of Electrochemical Science*, 11

(2016) 1121.
37. Y. Shen, F. Li, S. F. Li, D. B. Liu, L. H. Fan, Y. Zang, International Journal of Electrochemical Science, 7 (2012) 8702.
38. M. Sun, D. Z. Li, W. J. Li, Y. B. Chen, Z. X. Chen, Y. H. He, and X. Z. Fu, *Journal of Physical Chemistry C*, 112 (2008) 18076.
39. H. Z. Ma, B. Wang, X. Y. Luo, *Journal of Hazardous Materials*, 149 (2007) 492.
40. W. Y. He, X. N. Yan, H. Z. Ma, J. Yu, J. Wang, X. L. Huang, *Desalination and Water Treatment*, 51 (2013) 6562.
41. Y. Zhao, J. Chu, S. H. Li, Y. Chen, G. P. Sheng, Y. P. Chen, W. W. Li, G. Liu, Y. C. Tian, Y. Xiong, H. Q. Yu, *Chemical Engineering Journal*, 170 (2011) 440.
42. P. S. Liu, G. Cui, C. Y. Yang, *Materials Letters*, 155 (2015) 87.
43. W. Zhong, T. Jiang, Y. L. Dang, J. K. He, S. Y. Chen, C. H. Kuo, D. Kriz, Y. T. Meng, A. G. Meguerdichian, S. L. Suib, *Applied Catalysis A, General*, 549 (2018) 302.
44. G. Z. Li, G. Li, H. Wang, C. S. Xiang, J. D. Zhuang, Q. Liu, H. P. Tang, *Rare Metal Materials and Engineering*, 44 (2015) 1326.
45. M. H. Zhou, H Särkkä, , M Sillanpää. *Separation and Purification Technology*, 78(2011) 290.